Scientific Research Publishing

Optics and Photonics Journal, 2026, 16(2), 13-36
https://www.scirp.org/journal/opj
ISSN Online: 2160-889X
ISSN Print: 2160-8881

Shock Processes of Relaxed Optics: Modeling and Discussions

Petro Trokhimchuck

Anatolii Scvidzinskiy, Department of Theoretical and Computer Physics, Lesya Ukrainka Volyn' National University, Lutsk, Ukraine
Email: trope1650@gmail.com

How to cite this paper: Trokhimchuck, P. (2026) Shock Processes of Relaxed Optics: Modeling and Discussions. *Optics and Photonics Journal*, **16**, 13-36.
https://doi.org/10.4236/opj.2026.162002

Received: July 21, 2026
Accepted: August 22, 2026
Published: August 25, 2026

Abstract

Possible features of observing the shock processes in Relaxed Optics are analyzed and discussed. Along with acoustic shock processes, electromagnetic shock processes are also observed. The formal analogy between acoustic and electromagnetic shock processes follows from the specifics of the propagation of shock acoustic waves and Cherenkov radiation. The first process is limited by the speed of sound in the medium, while the second is limited by the phase speed of light in the medium. The speed of sound in a medium characterizes the speed of propagation of thermal vibrations of the medium, while the phase speed of light in a medium characterizes the speed of propagation of electromagnetic vibrations of the medium. In other words, these are characteristics of the collective motion of atoms, electrons, and ions of the medium. For the case of intense laser irradiation in the saturation regime of excitation, these considerations are also transferred to irreversible processes (instead of microvoids, nanovoids are observed in the experiment). If acoustic shock processes are characterized by the speed of processes that are greater than the speed of sound in the medium, then electromagnetic shock processes are characterized by the speed that is greater than the phase speed of light in the medium. Both the speed of sound and the phase speed of light in the medium are characteristics of collective acoustic and electromagnetic processes of the medium, respectively. From this point of view, there is a certain analogy, although the experimental implementations of these processes differ significantly. Two types of model are discussed: two-cascade acoustic and five-cascade electro magnetic. That is why we analyzed the specifics of modeling and observing these processes in different media: solids, liquids, and gases. For this purpose, a cascade model of optical breakdown of the medium was used, which includes a modified Rayleigh model (five-cascade model). The feasibility of using this model to describe and explain the presented experimental results is analyzed. It is shown that, by the size of the voids, we can judge the nature of laser-

induced shock processes: acoustic or electromagnetic.

Keywords

Cherenkov Radiation, Rayleigh Model, Optical Breakdown, Relaxed Optics, Mach Cone, Electromagnetic Shock Processes, Acoustic Shock Processes, Modeling

1. Introduction

Physics can be divided into several major branches such as optics, mechanics, electromagnetism, thermodynamics, and more recent branches including general relativity or quantum mechanics [1]-[5]. The distinguishing feature of each of these branches is the type of material behaviour they are concerned with, and consequently, the various laws that govern that behaviour. Acoustic Shock Physics is part of Classical Mechanics [6]-[13], in which laws can be expressed as mathematical equations and describe the conservation of certain values such as mass, energy, and momentum. The purpose of these general laws of mechanics is to explain how materials move when subjected to mechanical forces. More generally, mechanical engineers provide answers to the question, "how does a material change shape depending on the forces (or stresses) applied to it?" If we were to give a very general summary, we could say that mechanics is concerned with the way materials are deformed when subjected to forces.

Shock Physics is concerned with the same phenomena, but with one fundamental difference: the time during which the stress is applied (force per unit area). In other words, in the case of an impact (vehicle against a wall, block of ice on an aircraft cockpit, bullet on armour, space debris on a satellite, etc.) or explosive, the material is subjected to shock waves which transmit information about the stress imposed on a part of the material. The propagation times are relatively short, depending on the propagation speed of the shock waves within these materials. For example, in steel or aluminium, the propagation speed (also known as velocity of propagation) is around 5000 m/s, in ceramics approximately 10,000 m/s, and in plastics around 3000 m/s [1].

The main characteristic of Shock Physics is therefore the dynamics of the phenomena encountered, *i.e.*, the speed at which the material is deformed. The time scales dealt with here are microseconds or even nanoseconds. There is no need to be a genius to work out that a material will not react in the same way if it is subjected to forces for one μs or several seconds [1].

This is the real crux of Shock Physics: how to characterize a material's behaviour (deformation, damage, fragmentation) with respect to the intensity of the stress applied as well as the time during which it is applied [1].

In Relaxed Optics, along with acoustic shock processes, electromagnetic shock processes are also observed [1] [2].

The formal analogy between acoustic and electromagnetic shock processes follows from the specifics of the propagation of shock acoustic waves [6]-[13] and Cherenkov radiation [14]-[16]; the latter is limited by the phase speed of light in the medium. The speed of sound in a medium characterizes the speed of propagation of thermal vibrations of the medium, while the phase speed of light in a medium characterizes the speed of propagation of electromagnetic vibrations of the medium. In other words, these are characteristics of the collective motion of atoms, electrons, and ions of the medium. For the case of intense laser irradiation in the saturation regime of excitation, these considerations are also transferred to irreversible processes (instead of microvoids, nanovoids are observed in the experiment) [1]-[4].

If acoustic shock processes are characterized by the speed of processes that are greater than the speed of sound in the medium [6]-[13], then electromagnetic shock processes are characterized by the speed that is greater than the phase speed of light in the medium [1]-[4]. Both the speed of sound and the phase speed of light in the medium are characteristics of collective acoustic and electromagnetic processes of the medium, respectively. From this point of view, there is a certain analogy, although the experimental implementations of these processes differ significantly.

As an example of acoustic shock processes, a model of material deformation processes induced by laser-generated shock waves is analyzed. These results were obtained for copper and aluminum after irradiation with a series of third harmonic nanosecond pulses of an Nd laser [13]. A two-cascade model was created: the first step is the generation and propagation of shock waves, and the second is the relaxation of the irradiated matter [13].

That is why we analyzed the specifics of modeling and observing these processes in different media: solids, liquids, and gases. For this purpose, a cascade model of optical breakdown of the medium was used, which includes a modified Rayleigh model or, in a more general sense, a five-cascade model [1]-[5]. The feasibility of using this model to describe and explain the presented experimental results is shown.

Based on these results, a criterion was formulated for determining the nature of shock processes by the size of laser-induced voids: acoustic (microvoids) and electromagnetic (nanovoids).

2. Wave Shock Processes and Acoustic Case

Consider a stationary homogeneous gas flow that moves at a speed V relative to a stationary frame of reference S. If the speed V of the flow exceeds the speed c of sound in the gas (relative to the gas itself), then the flow is called supersonic; if V is less than c, then the flow is called subsonic. The properties of a supersonic flow are significantly different from the properties of a subsonic flow. In this regard, an important flow characteristic is the ratio M of the flow speed to the speed of sound in it [6]:

$$M = \frac{\boldsymbol{V}}{c}. \tag{1}$$

This number is called the Mach number.

One of the features of a supersonic flow is that small perturbations of gas density (and other quantities) cannot propagate in any direction in such a flow. Indeed, the speed of propagation of disturbances relative to S is equal to the sum $\boldsymbol{V} + v_s \boldsymbol{n}$, where $\boldsymbol{n}$ is the direction of propagation of disturbances relative to the gas, v_s is the speed of sound in the medium. Therefore, all possible velocities of propagation of disturbances relative to S can be obtained if the vector is set aside from the fixed point O (at which the disturbances occur) and $\boldsymbol{V} + v_s \boldsymbol{n}$, if fixed V, all possible directions are given to the vector $\boldsymbol{n}$. As a result of such a vector change, the end of the vector $\boldsymbol{V} + v_s \boldsymbol{n}$ will be tangent to a sphere with radius c centered at the end of the vector V (**Figure 1**) [1]-[3] [6].

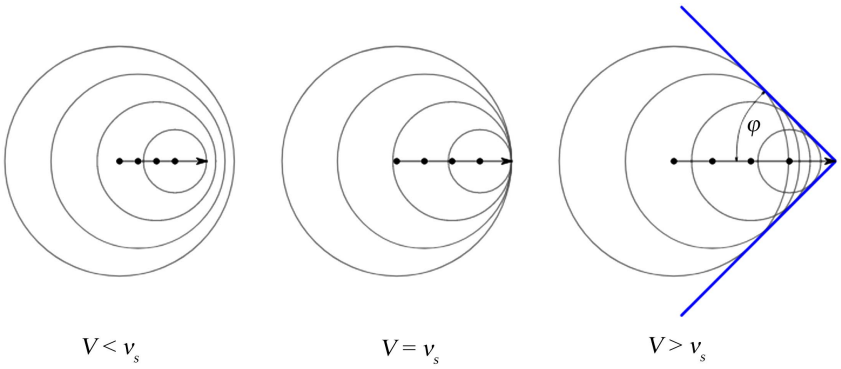

Figure 1. The emergence of a Mach cone. When a body moves in a medium at subsonic speeds ($V < v_s$), sound waves overtake the moving body; at transonic speeds ($V = v_s$), a density jump occurs in front of the moving body; at supersonic speeds ($V > v_s$), the enveloping system of sound waves forms a Mach cone (V is the flow velocity, v_s is the sound velocity) [1] [3] [4] [6].

A model of material deformation processes induced by laser-generated shock waves is analyzed in [13]. The processes include laser peen forming (LPF) and laser shock peening (LSP) of metals. Numerical solutions of the model using the finite element method were implemented in two steps: 1) explicit step, devoted to shock wave propagation, and 2) implicit step, calculating relaxation of the material. A series of LPF and LSP experiments was conducted to validate the model. The residual stress measurements by synchrotron X-ray diffraction and deformation measurements by profilometry showed that the experimental and numerical results were in good agreement. It is the first time that the novel process of micro-scale LPF has been studied numerically and experimentally. An important aspect of the work is that the numerical results were further analytically explored to gain improved understanding of wave-solid interaction, including shock wave attenuation and shock velocity variation [13].

Shock waves are characterized in that the wave front, in which compression takes place, is a region of sudden and violent change in material velocity, stress,

and density. Since the experiments in the 1960s utilizing high-power pulsed lasers to generate shock waves in solid targets, the laser shock technique has led to many investigations, including laser peen forming (LPF) and laser shock peening (LSP), as shown in Figure 2 [13].

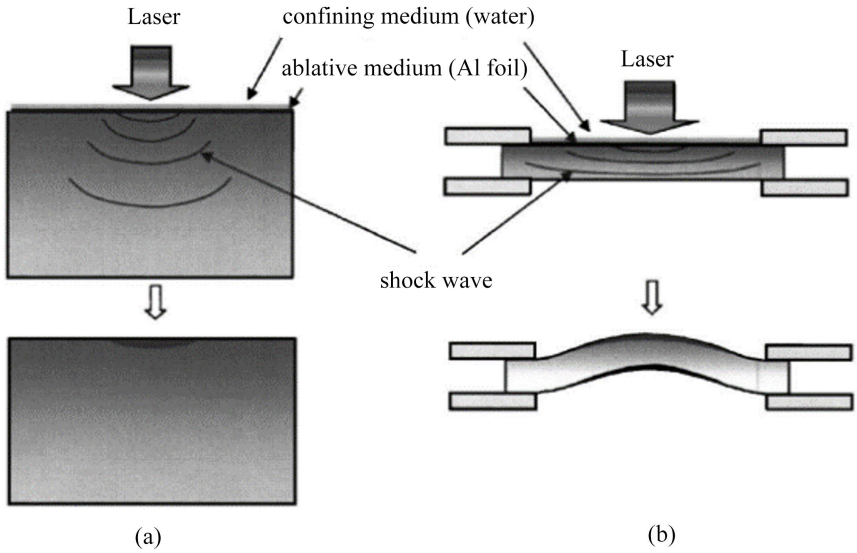

Figure 2. Material deformation processes induced by laser-generated shock waves: (a) laser shock peening (LSP) (LSP causes compressive residual stress on the processed surface) and (b) laser peen forming (LPF) [13], (LPF forms the sheet, imparting compressive residual stress on both surfaces).

Laser-generated shock waves result from the expansion of a high-pressure plasma caused by a pulsed laser. An intense laser pulse interacting with a solid target immediately causes the surface layer to instantaneously vaporize into a high-temperature and high-pressure plasma. This ablated plasma expands from the surface and, in turn, exerts mechanical pressure on the face of the target, which induces compressive waves in the solid target, and therefore a shock wave is propagated through the sample. If it is confined by liquid or another type of laser-transparent medium, the shock pressure can be magnified by a factor of 5 or more compared with the open-air condition. The coating also protects the target from thermal effects so that nearly pure mechanical effects are induced. LSP is a process in which beneficial compressive residual stress is imparted into the processed surface layer of metal or alloy parts by laser-generated shocks, and the process has been extensively investigated and in some cases successfully applied. When the peak pressure created by the shock wave is above the dynamic yield stress [Hugoniot elastic limit (HEL)] of metal, the metal is plastically deformed at the surface which will induce compressive residual stress in the surface of the part and thus increase the resistance of the metal to surface-related failures such as fatigue, fretting fatigue, and stress corrosion cracking. LSP is only a surface treatment method, and does not produce appreciable change of shape. LPF is a process involving laser-generated shock waves. It combines the beneficial effects (compressive resid-

ual stresses on the surface) of a LSP with a controlled bending deformation, to shape parts [7] [13]. The process is more effective than other thermal-forming methods with a distinct advantage that surface stresses generated can be compressive. Therefore, the process results in increased fatigue resistance of the target material in addition to shaping it. However, to advance LSP and LPF, in particular, the answers to some questions, for example, how to control the repetition rate in a multiple-pulsed laser processing, how to determine the pulse duration considering the thickness of parts during LPF, and in two-sided LSP, how to design the phase difference between the two shock waves in order to gain an optimal effect, need to be further investigated [13]. These questions are closely related to the shock-solid interactions, such as shock wave attenuation and reflection and variation of shock wave velocity.

A model was previously developed for the prediction of laser-generated pressure in the confined ablation mode. [16] It considered the mass, energy, and momentum exchanges between plasma and the confining medium or between plasma and the metallic target. The expansion of the plasma was modeled as a one-dimensional laser-supported combustion wave. **Figure 3** presents the calculated laser-generated shock loading profiles under different processing conditions [13]. The calculated shock loading was assumed to be of a spatially Gaussian distribution and would be used in the later shock wave propagation simulation as input shock loading.

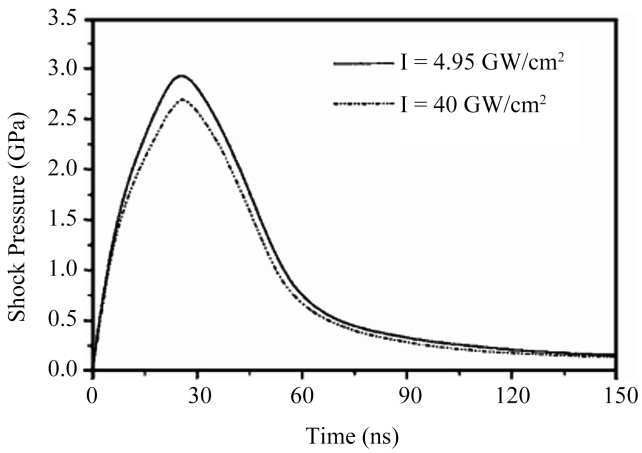

Figure 3. The loading history based on a former model [13].

The precise numerical description of an LPF or LSP process requires the simulation to take into account the hydrodynamic behavior of the material and the deviatoric behavior considering work hardening and strain rate effects. When the applied stress greatly exceeds the yield stress of a solid, material behavior is more complicated, and can be approximated by a fluidlike one because the fractional deviations from stress isotropy are small. The complete process of shock wave propagation in solids should be governed by the three conservation equations, and the equation of state that can be expressed in terms of specific internal energy as

a function of pressure and density for the hydrodynamic behavior of the material, and the elastic-plastic constitutive relation for deviatoric behavior [13].

In the calculation of the elasto-plastic behavior, the stress-tensor components are divided into a hydrostatic equation of state and an elastic-plastic constitutive model.

The stress components σ_{ij} can be written as

$$\sigma_{ij} = -P + s_{ij}, \tag{2}$$

where P is the hydrostatic pressure and s_{ij} are the deviatoric stress components [13].

A commonly used equation of state for solids is the Mie-Grüneisen equation of state. The Mie-Grüneisen equation of state, which establishes a relationship between pressure P and internal energy E with reference to the material Hugoniot curve, was used,

$$P - P_H = \gamma_0 \rho_0 \left(E - E_H \right), \tag{3}$$

where P_H and E_H are the Hugoniot pressure and internal energy, γ_0 is a material constant, and ρ_0 represents the initial-state density.

The Hugoniot curve is described by the linear relation between the shock velocity v_S and particle velocity u with coefficients from experimental data.

$$U = C_0 + Su, \tag{4}$$

where the constant C_0 is the sound speed at zero pressure, and the material constant S has a value between 1.0 and 1.7 for most metals [13] [17].

Combining Equation (4) with the Rankine-Hugoniot jump conditions [13], the Hugoniot pressure and internal energy can be obtained as follows:

$$P_H = \frac{\rho_0 C_0 h}{\left(1 - Sh\right)^2}, \tag{5}$$

$$E_H = \frac{P_H \eta}{2\rho_0}, \tag{6}$$

However, on the basis of a composite model, 25 local strain and residual stress can be evaluated for metals under plastic.

The deformation, based on the fact that crystal dislocations often arrange themselves into a cellular structure after impact loading. In the model, the deformed crystal is considered as a two-component system, where the local flow stress of the cell walls is considerably larger than the local flow stress of the cell interiors. Consequently, in the plastically deformed and unloaded crystals, the cell walls parallel to the compressive axis are under a residual uniaxial compressive stress $\Delta\sigma_w < 0$ and the cell interior under a uniaxial tensile stress $\Delta\sigma_c > 0$. The asymmetrical Bragg reflections can be separated into the sum of two symmetrical peaks, which correspond to "cell interiors" and "cell walls" as postulated by Ungar *et al.* The centers of both components are shifted in opposite directions in accordance with $\Delta\sigma_w < 0$ and $\Delta\sigma_c > 0$. Then, the measure of the residual stresses can be characterized by the absolute value of the difference in the following:

$$\sigma_{zz} = \left|\Delta\sigma_w - \Delta\sigma_c\right| \tag{6a}$$

The lateral residual stress in the sample surface plane is

$$\sigma_{xx} = \sigma_{yy} = -\sigma_{zz}\nu\,, \tag{6b}$$

where ν denotes Poisson's ratio.

Now, substituting Equations (6a) and (6b) into Equation (6) yields the following [13].

$$P = \frac{\rho_0 C_0 h}{(1-Sh)^2}\left(1-\frac{\gamma_0 h}{2}\right)+\gamma_0\rho_0 E, \tag{7}$$

where $h = 1 - \rho_0/\rho$, and ρ is the density. Equation (7) is the final form of the equation of state to be used in this simulation. In the following numerical modeling of shock-solid interactions, work hardening, strain rate, and pressure effects on yield strength are considered, while temperature is taken as room temperature. This is reasonable because only the coating is vaporized and minimal thermal effects are felt by the sample. The solid target is assumed to be isotropic.

All experiments were conducted by a frequency-tripled Q-switched Nd: yttrium aluminum garnet (YAG) laser with a wavelength of 355 nm in TEM_{00} mode. The pulse duration was 50 ns, and the pulse repetition rate could vary between 1 and 20 kHz. The laser beam diameter is 12 μm and the laser intensity was varied from 2 to 6 GW/cm^2 [13].

For LPF, copper stripes with a thickness of 100 μm were used as samples. These stripes were cut to 20 × 3 mm^2 using a wire electric discharge machine (EDM), and then heat-treated and electropolished to relieve residual stress. Then, a thin layer of high-vacuum grease (about 10 μm) was spread evenly on the polished sample surface, and the ablative medium, aluminum foil of 16 μm thick, was tightly pressed onto the grease. These stripes were clamped at both ends, leaving 10 mm length in the middle unsupported for LPF experiments. Caution was exercised to prebending effects and to ensure that these stripes remain flat during these steps [13].

For LSP, well-annealed pure aluminum samples in the dimensions of 15 × 10 × 5 mm^3 were used. The sample preparation was the same as introduced before. The setups for LPF and LSP are schematically shown in **Figure 2** [13].

For both LPF and LSP, the laser process procedure is similar. The samples were placed in a shallow container filled with distilled water around 3 mm above the sample top surface. A series of laser pulses was applied along the width direction (the dimension of 3 mm for LPF and the dimension of 10 mm for LSP) with 25 μm spacing between adjacent pulses. This forms an approximately uniformly deformed straight shocked line [13]. Pulse energies of 226 and 280 μJ corresponding to laser intensities of 4.0 and 4.95 GW/cm^2 were used for LPF and LSP, respectively. After shock processing, the coating layer and the vacuum grease were dissolved in acetone solution, and the shock-induced deformation and residual stresses on the samples were measured. The conditions and the mechanical properties of the studied materials are summarized in **Table 1** and **Table 2**, respectively.

Table 1. Samples and experimental conditions for LPF and LSP [13].

	Material	Sample size (mm^3)	Laser intensity (GW/cm^2)	Pulse energy (μJ)
LPF	Cu	10 × 3 × 0.1	4.95	280
LSP	Al	15 × 10 × 5	4.0	226

Table 2. Mechanical properties of the studied materials [13].

	p_0 (kg/m^3)	G (MPa)	γ	C_0 (m/s)	S
Cu	9860	468	1.99	3940	1.489
Al	2700	262	2.0	5386	1.34

The samples are mounted on a translation stage with a positioning accuracy of ±1 μm in the x and y directions in the sample surface. Monochromatic synchrotron radiation at 8.0 keV (λ = 1.540 24 Å) is used, since it is smaller than the K absorption edges for Al and Cu which are 8.98 and 8.3 keV, so that the fluorescence radiation would not be excited [13].

Multiple measurement points were chosen along a line perpendicular to the shocked line. The spacing between adjacent measurement points starts from 20 μm (when ±100 μm away from the center of the shocked line) and reduces to 5 μm within ±20 μm from the center of the shocked line in order to spatially resolve the residual stress. At each position, the corresponding x-ray diffraction profile is recorded and repeated for each shocked line. For LSP, only the shocked surface was measured, while for LPF, residual stress measurements on both the top and bottom surfaces were conducted. It should be noted that the penetration depths of x ray in copper is about 10 μm and in aluminum around 40 μm. Therefore, the measured residual stress is an average in the depth [13].

The comparison between the measured deformation of the copper stripe after LPF and the numerical result predicted is shown in **Figure 4**. Before laser peen forming, the stripe slightly curves upward with the center of the stripe raised by about 5 μm. After LPF, the stripe bent upward further, and the shocked area was raised by up to 10 μm. The numerically predicted deformation and the experimental results are in good agreement.

The comparisons of the residual stress distributions on both the top and bottom show that the numerically predicted distribution matches the experimental results very well. The modeled residual stress distribution and the bending induced by LPF of the copper stripe are also shown in **Figure 5** [13]. When high pressure was applied to the copper, the shocked material tended to flow away from the shocked center and caused elongation of the top layer of the stripe, which led the stripe to bend up, and meanwhile induced compressive residual stress on the bottom surface and, because of spring back and shock compression, the top surface.

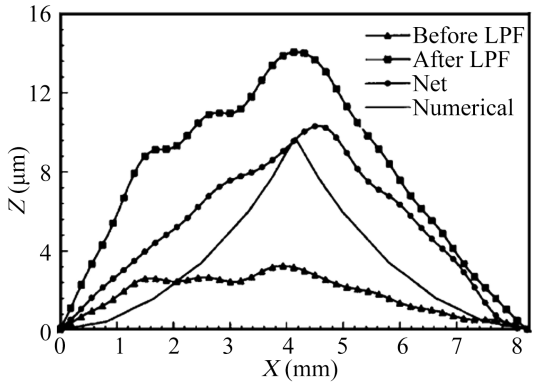

Figure 4. Comparisons of the deformation after LPF between the experimental and numerical results [13].

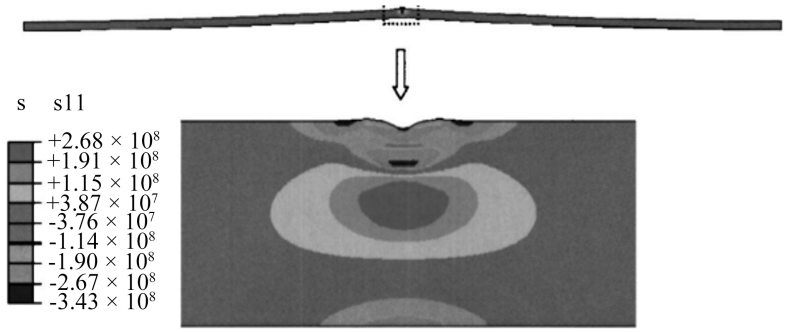

Figure 5. The simulated deformation and residual stresses field is induced by LPF. The deformation of the stripe is magnified ten times for viewing clarity [13].

Figure 6 shows the comparison between the AFM-measured dent on the shocked area after LSP of the bulk aluminum sample and the FEM calculated result. The x-ray-microdiffraction-measured residual stress distribution induced by LSP and the numerically obtained residual stress field are shown in **Figure 7**. The calculated residual stresses for comparison in **Figure 6** and **Figure 7** are averaged over the penetration depth of X-ray [13] [18]. Both **Figure 6** and **Figure 7** show good agreement between the experimental and numerical results.

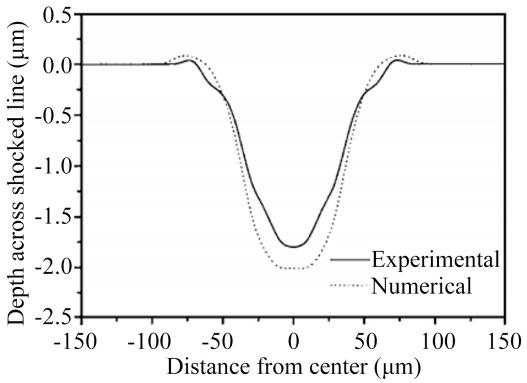

Figure 6. Comparison of the measured and simulated dents across the shocked line after LSP of the Al sample [13].

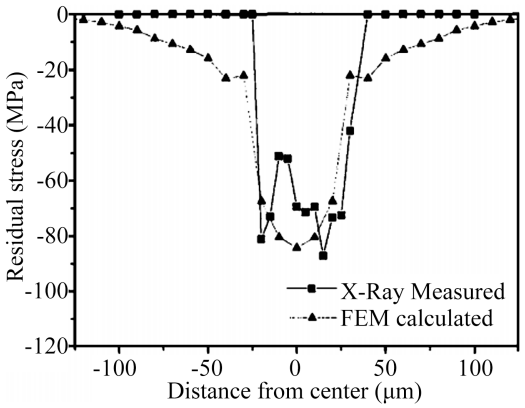

Figure 7. Comparison between the measured residual stresses distribution induced by LSP on the shocked surface of the Al sample with the numerical result [13].

3. Creation of Laser-Induced Voids and Electromagnetic Case

In contrast to the previous case, we will now consider the case of the formation of laser-induced shock processes at absorption coefficients of incident radiation with absorption coefficients of 10^{-3} - 10^{-1} cm^{-1} [1]-[5]. It is the laser-induced breakdown of matter.

Experimental data, which include the microscopic structure of optical breakdown in 4H-SiC (silicon carbide), are presented in **Figure 8** and **Figure 9** [19] [20]. The sectional area of the receiving structures was ~22 μm, with a depth of ~50 μm. As seen from **Figure 8(c)**, we observe five stages of disordered regions, which are located at a distance of 2 to 4 μm apart vertically [19] [20]. The branches themselves in this case have a thickness from 150 to 300 nm. In this case, there are lines in the irradiated nanocavity with a spherical diameter from 10 nm to 20 nm. In this case, the irradiated structures have the crystallographic symmetry of the initial structure.

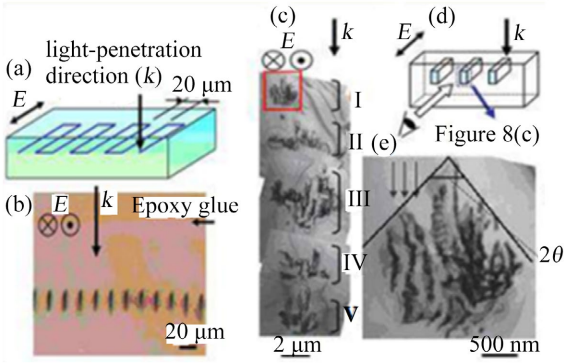

Figure 8. (a) Schematic illustration of the laser-irradiated pattern. The light propagation direction (*k*) and electric field (*E*) are shown. (b) Optical micrograph of the mechanically thinned sample showing cross sections of laser-irradiated lines (200 nJ/pulse). (c) Bright-field TEM image of the cross section of a line written with a pulse energy of 300 nJ/pulse. (d) Schematic illustration of the geometric relationship between the irradiated line and the cross-sectional micrograph. (e) Magnified image of a rectangular area in (c) [9] [10].

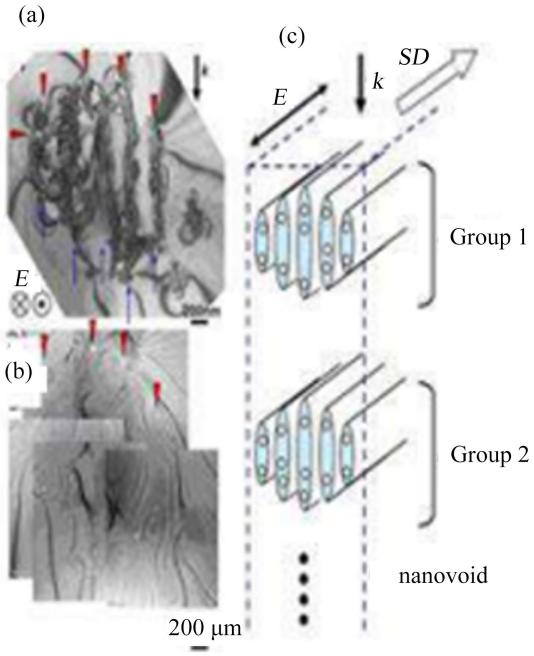

Figure 9. Laser-modified layers with a spacing of 150 nm are indicated by arrows. (a) Bright-field TEM image of a portion of the cross section of a line written with a pulse energy of 200 nJ/pulse. (b) Zero-loss image of the same area as in (a), with nanovoids appearing as bright areas. Correspondence with (a) is found by noting the arrowheads in both micrographs. (c) Schematic illustrations of the microstructure of a laser-modified line. Light-propagation direction (*k*), electric field (*E*), and scan direction (SD) are shown. Only two groups (groups I and II) of the laser-modified microstructure are drawn [9] [10].

In this case, diffraction processes may be generated in two stages: 1—formation of diffraction rings of focused beams [19] [20], and second-formation of diffracting gratings during the redistribution of second-order Cherenkov radiation [2]. The second case is analogous to the creation of self-diffraction gratings in Nonlinear Optics, but for **Figure 8(c)** and **Figure 9(b)**, our gratings are limited by the Mach cone of Cherenkov radiation. Roughly speaking, only **Figure 8(e)** and **Figure 9** represent "clean" shock processes (breakdown) [2].

Since the initial radiation is focusing, it causes the occurrence of heterogeneous polarization of the medium, which in turn is the source of the generation of a whole range of non-linear optical effects, leading to a continuous spectrum [3] [6]. However, since the cone of initial radiation is transformed into a set of diffractionally stratified cones of heterogeneous polarization of the medium, the radiation then occurs inside the cones, the generators of which are perpendicular to the generator cones of polarization. In addition, this, according to [16] [21], is Cherenkov radiation.

For the explanation of the experimental data of **Figure 8** and **Figure 9**, the following cascade of processes was used: diffraction stratification of the initial radiation; generation of Cherenkov radiation; interference of the short-wave of this Cherenkov radiation and optical breakdown at the maximum of the corresponding interferogram [2].

The estimation of the sizes of the cascade of volume destructions in **Figure 8(c)** may be explained in the following way [1]-[5]. The sizes (diameters) of the proper stages d_{nir} of the cascade are proportional to the corresponding diffraction diameters d_{ndif}

$$d_{nir} = kd_{ndif}, \tag{8}$$

where k is the proportionality constant.

The diffraction diameters d_{ndif} may be determined with the help of the condition of diffraction-pattern lobes (modified Rayleigh ratio).

$$d_{ndif} = n\lambda. \tag{9}$$

The estimations of the first five diffraction diameters d_{ndif} for λ = 800 nm were presented in [2]. The Cherenkov angle may be determined from the following formula [1]-[5].

$$\theta_{ch} + \alpha_{ir} = \frac{\pi}{2} \quad \text{or} \quad \theta_{ch} = \frac{\pi}{2} - \alpha_{ir}, \tag{10}$$

where α_{ir} –angle between the tangent line and the direction of the laser beam (focusing angle).

The last formula was received on the basis of A. Bohr's microscopic theory of Cherenkov radiation [21]. According to this theory, each electron has its own zone of influence in the irradiated medium (A. Bohr hyperboloid, **Figure 10** [21]).

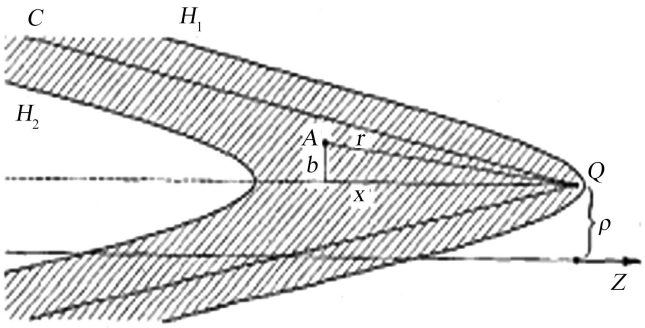

Figure 10. To explain a deceleration of a particle in matter (A. Bohr hyperboloid) [21].

Now we receive an estimation of the interaction of an electron, which is placed at point Q and collides with particle Z that is transmitted over a distance of ρ (**Figure 10**) [21].

Simultaneously other accelerated electrons mainly in time $t' = t - \frac{r}{c}$ after a collision from this particle. An electron at point A at moment t' was placed in phase of cocollision, which is advanced in time τ the phase of cocollision at point Q. A time τ is equaled [21]

$$\tau = \frac{r}{c} - \frac{x}{v} \tag{11}$$

where v–the velocity of the particle, x–the projection of the distance QA in the direction of motion.

Introductive $r^2 = x^2 + b^2$ we received from Formula (11) the next correlation [21]

$$\frac{\left(x+v\tau\gamma^2\right)^2}{v^2\tau^2\gamma^2\left(\gamma^2-1\right)}-\frac{b^2}{c^2\tau^2\left(\gamma^2-1\right)}=1. \tag{12}$$

where $\gamma=\left(1-\frac{v^2}{c^2}\right)^{-1/2}$.

Generally speaking, the Bohr hyperboloid can be considered a hyperboloid of the polarization of the medium [2] [21]. Under appropriate conditions, the generators of the Cherenkov radiation cone are perpendicular to the surface of the hyperboloid. Moreover, this applies to each incident particle. In the case of irradiation with focused laser radiation, the role of O. Bohr hyperboloids is played by diffraction stratified cones of focused laser radiation [1]-[4]. If for electrons the number of cones (hyperboloids) is determined by the number of incident particles, then for focused laser radiation–by the number of stratified cones (this is confirmed by the experimental results of **Figure 8**). In this case, the generators of the Cherenkov radiation cones will be perpendicular to the generating diffraction cones [3]. Thus, we have optically induced Cherenkov radiation, the photon efficiency of which is ~0.2 - 0.5, while for classical Cherenkov radiation it is ~10^{-7} - 10^{-5}. For the optical case, the radiation energy goes mainly to the polarization of the medium, while when irradiated with high-energy particles, the main part of the energy goes to radiation defect formation (displacement of atoms, etc.) [1]-[5].

It should be noted that laser-induced continuous and cone radiation is nothing more than optically induced Cherenkov radiation [1]-[5] [16].

It was noted that cone radiation has a surface structure. From our point of view, this is explained by the fact that the main role in the formation of Cherenkov radiation is played by diffraction cones [1]-[5]. The polarization processes that lead to Cherenkov radiation occur in the near-surface regions of these cones; therefore, the resulting radiation has a surface nature [1]-[5].

We can roughly estimate basic peculiarities of energy distribution in a Mach cone using the following formula [2].

$$E_{1ob}=\frac{\pi^2}{4}\left(\sum_{i=1}^{5}n_{iav}^2 l_{iav}\right)r^2 N_{aSiC}E_{Zth}, \tag{13}$$

where n_{iav} is the average visible number of filaments in the appropriate group of the cascade, l_{iav} = 1000 nm is the average length of filaments in the appropriate group of the cascade, r = 10 nm is the average radius of the filament, N_a is the atom density of 4H-SiC.

For further estimation, we use the next approximation $n_{1av} = n_{2av} = n_{3av} = n_{4av} = n_{5av}$ = 100 (see **Figure 8(c)**) [3].

Energy, which is necessary for the optical breakdown of our nanotubes, may be determined in the following way. Zeitz threshold energy for 4H-SiC is equal to

E_{Zth} ~ 25 eV [3]. Let this value correspond to the energy of optical breakdown. Therefore, the total energy E_{1ob} is equal to

$$E_{1ob} = N_{asnt} \cdot E_{Zth} = 23.2 \text{ nJ}. \tag{14}$$

This value is equal to ~8% of the pulse energy or ~30% of the effective absorbed energy of the pulse [2]. In this case, we have a higher efficiency of transformation of initial radiation to the "irreversible" part of Cherenkov radiation. This is the result of more intensive excitation compared with classical methods of generating Cherenkov radiation. In this case, we have purely photochemical processes. The experimental data for intrinsic absorption [2] show that for the short pulse regime of irradiation (femtosecond regime), the basic processes of destruction in fused silica and calcium fluoride are photochemical (multiphoton absorption in the regime of excitation saturation). However, the main peculiarity of the experimental data in **Figure 2** and **Figure 3** is the transformation of the initial laser radiation (wavelength 800 nm) to continuum Cherenkov radiation. From the length of optical breakdown in 4H-SiC, we can determine the average absorption index of Cherenkov radiation. It is ~10^4 cm^{-1}. This value corresponds to the violet-blue range of the absorption spectrum of 4H-SiC [1]-[5].

For the estimations of the maximal radius of nanovoids, we must use the modified Rayleigh formula [1]-[5] [22]-[24].

$$R_{max} = \frac{2R}{0.915r}\sqrt{\frac{E_{ir}}{\pi\tau_{ir}cE}}, \tag{15}$$

where T_c is the time of creation of the nanovoid (bubble), R is the radius of nanovoid, r is the radius of the irradiated zone, E is the Young's modulus, E_{ir} is the energy of one pulse. τ_{ir} is the duration of the pulse [2]. Here we introduced the pressure of light [2] [23] [25].

If we substitute r = 250 nm, R = 10 nm, E = 600 GPa [1]-[5], E_{ir} = 300 nJ, τ_{ir} = 130 fs, $c = 3 \times 10^8$ m/s, then we have R_{max} = 11 nm [1]-[5].

The speed of shock waves for the femtosecond regime of irradiation is less than the speed of sound. However, we have two speeds of sound in an elastic body: longitudinal v_{ls} and transversal v_{ts} [1]-[5]. Their values are determined by the following formulas.

$$v_{ls} = \sqrt{\frac{E(1-\nu)}{\rho_0(1+\nu)(1-2\nu)}}, \text{ and } v_{ts} = \sqrt{\frac{E}{\rho_0(1+\nu)}} \tag{16}$$

where ν is Poisson's ratio [1] [2]. The ratio between these two speeds is equaled

$$\alpha = \frac{v_{ts}}{v_{ls}} = \sqrt{\frac{1-2\nu}{2(1-\nu)}}. \tag{17}$$

However, this ratio must also be valid for shock waves. Therefore, for silicon carbide with ν = 0.45 [3], α = 0.33. Roughly speaking, the last ratio determines the step of the ellipsoidal forms of our nanovoids (**Figure 9(c)**).

Formulas (16) allow estimating maximal longitudinal and transversal R_{maxi}, $i \in (l,t)$. These values are 6 nm and 19 nm, respectively, for SiC [2].

In a similar manner, the results of the optical detection of potassium chloride when irradiated with nanosecond pulses of a CO_2 laser [11] were evaluated.

Laser-induced optical breakdown was researched in [1] [2] [26]. Two damage regions in a crystal with a moderately high density of inclusions were observed in [26] for potassium chloride after irradiation by CO_2-laser pulses (wavelength 10.6 μm, pulse duration 30 ns). The laser was known to operate in the lowest-order transverse Gaussian mode. There were several longitudinal modes, however, which contributed a time structure to the pulse, periodic at the cavity round-trip time. The phase relationships between the longitudinal modes varied from shot to shot, changing the details of the time structure and causing the peak of the envelope to fluctuate by ±15% [26]. These results are presented in **Figure 11** [26].

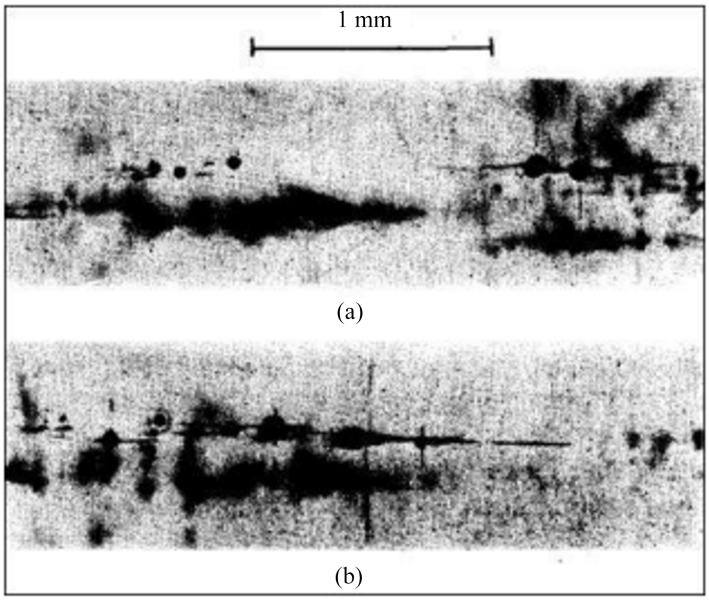

Figure 11. Two damaged regions in a crystal KCl with a moderately high density of inclusions. The round black objects are bubbles. The radiation, incident from left to right, was just at the intrinsic breakdown threshold. In one case (a), there was damage only at the inclusions. In (b), intrinsic breakdown occurred, as evidenced by the pointed bubble. The straight lines represent cleavage [26].

Successive laser shots (1/sec) were focused into bulk single crystals using a 1-inch focal length "Irtran 2" lens. The breakdown was monitored by observing the visible light from the focal region and by examining the damaged region under the microscope. It was found that most of the crystals suffered some damage even at relatively low power levels. The threshold of this type of damage varied by an order of magnitude from one position in the crystal to another. At any particular energy level, damage would occur on the first laser shot or not at all. **Figure 11(a)** shows that spatial inhomogeneities are in fact inclusions [26]. The damage bubbles occur randomly near, not necessarily in, the tiny focal volume. At a well-defined power threshold, an elongated pointed bubble forms, its vertex falling at the focus (**Figure 11(b)**). This power level is regarded as the bulk intrinsic breakdown

threshold. Its value is reproducible in crystals from different manufacturers, with inclusions or without. When no inclusion-free samples of a compound were available, the considerations mentioned above were used to determine the dielectric strength [26].

Let us take the ratio of the radius of the irradiation zone to the radius of the nanowire as 50 [13]. The energy of irradiation is 2 J. The duration of irradiation is 30 ns, and the mode of CO_2-laser irradiation is TEM_{01} [2] [25]. Young's modulus is 29.67 GPa, and Poisson's ratio is 0.216 [2]. In this case, due to the mode structure of the irradiation, we had two breakdown channels, each with ~7 cascade members (**Figure 11**). However, we do not see the microscopic breakdown structure here due to the low resolution of the optical photograph compared to the TEM images of **Figure 8** and **Figure 9**. Experimental data for KCl (**Figure 11**) and for SiC (**Figure 8(c)**) have similar appearances [2].

Therefore, in a similar manner, the results of the optical breakdown of potassium chloride when irradiated with nanosecond pulses of a CO_2 laser [1]-[4] were evaluated. After substituting the corresponding data into Formula (15), we have $R_{maxKCl} = 62.5$ nm [1]-[4]. Ellipticity of KCl nanovoids may be determined from (17): $\alpha_{KCl} = 0.6$ [1]-[4].

Let us now estimate the maximum bubble radii for the acoustic case. For this, in Formula (15), you need to change the speed of light to the speed of sound (15a).

$$R_{max}^{ac} = \frac{2R}{0.915r}\sqrt{\frac{E_{ir}}{\pi\tau_{ir}v_s E}}, \tag{15a}$$

where v_s is the speed of sound.

As a result, we get $R_{maxSiC}^{ac} = 1.7$ μm and $R_{maxKCl}^{ac} = 28$ μm [1]-[4]. The shape of the voids does not change; they just increase in size by 2 - 3 orders of magnitude.

If we take the ratio of the acoustic Formula (15a) and the optical Formula (15), then for the same irradiation modes we have the ratio

$$\frac{R_{max}^{ac}}{R_{max}} = \sqrt{\frac{c}{v_s}}. \tag{18}$$

However, a comparison with the experimental results (**Figure 9**) shows that the main role in the formation of nanovoids is played mainly by electromagnetic processes. This is explained by the fact that, in this case, a chain of close-range coherent processes of transformation of both optical radiation into the excitation of the medium and the corresponding relaxation of the medium is implemented; in other words, there is a chain of interconnected coherent transformations.

To estimate the size of laser-induced micro- or nanowires in liquids and gases [24] [27]-[31], we can also use Formula (15), in which we need to replace Young's modulus E with the compressibility modulus K of the medium [1] [3] [4].

We have, for the electromagnetic case, the following formula

$$R_{maxel} = \frac{2R}{0.915r}\sqrt{\frac{E_{ir}}{\pi\tau_{ir}cK}}, \tag{15b}$$

and the acoustic case

$$R_{maxac} = \frac{2R}{0.915r}\sqrt{\frac{E_{ir}}{\pi\tau_{ir}v_s K}}. \tag{15c}$$

Therefore, we have

$$\frac{R_{maxliq}}{R_{maxsol}} \sim \sqrt{\frac{K}{E}}. \tag{19}$$

So, for equivalent regimes of irradiation

$$\frac{R_{maxH_2O}}{R_{maxSiC}} \sim \sqrt{\frac{600}{2.2}} = 16.51, \tag{19a}$$

and

$$\frac{R_{maxH_2O}}{R_{maxKCl}} \sim \sqrt{\frac{29.67}{2.2}} = 3.67. \tag{19b}$$

A compressibility modulus K for H_2O equals 2.2 GPa [28], and for air, 10^{-4} GPa [29]. Therefore,

$$\frac{R_{maxair}}{R_{maxSiC}} \sim \sqrt{\frac{600}{10^{-4}}} = 2450. \tag{19c}$$

Thus, the estimated sizes of "electromagnetic" water and air voids (radii) are 165 nm for water and 24.5 μm for air. The corresponding "acoustic" radii are approximately 74 μm for water and approximately 22.9 mm for air [3] [4].

Similar experimental results have been obtained for liquids and gases.

We conducted experimental studies of the interaction of a 30-μm-diameter droplet with laser radiation in the region where filamentation was observed. It was experimentally discovered that at high laser intensities, achieved near the laser filament, breakdown occurs on the droplet surface on the side where the laser pulse is incident, not just at its internal foci (**Figure 12(a)**) [31], with the droplet diameter being 30 μm. Furthermore, hot plasma hotspots–white light sources–were observed at the rear and front foci located within the droplet, as well as in the air, near the focal point located behind the spherical droplet (**Figure 12(b)**) [31]. An explosion of the water droplet, characterized by rapid dispersal of its substance, was experimentally observed.

(a) (b)

Figure 12. (a) Ionization of the front surface of the droplet, laser radiation propagates from left to right; (b) Plasma foci are formed in two internal foci of the droplet and behind [31].

The interaction of laser radiation was studied numerically using a self-consistent model. Maxwell's equations were solved using the FDTD method in combination with the electron density balance equation. It was shown that ionization on the front surface of the droplet occurs at incident radiation intensities of approximately 2.5×10^{13} W/cm^2. The region of laser energy absorption by the droplet substance has a complex structure due to the interference of radiation propagating within the droplet with its reflections within the droplet. The greatest amount of energy is released near the focal point near the rear wall of the droplet (located further downstream of the radiation path), while less energy is released near the front wall. At high intensities in the incident pulse, when ionization occurs on the front surface of the droplet and above, the quantitative ratio of energy deposits changes.

The spectral and angular properties of the conical radiation are well-known [30]. The cone angle is 1˚ - 3˚ and increases as the laser frequency approaches the atomic transition and with increasing sodium density. The cone spectrum is broad (5 - 10 cm^{-1}) and is to the red of the transition. For small laser detuning (5 - 10 cm^{-1}), the peak of conic emission is detuning. For large laser detuning (6 - 20 cm^{-1}), the peak detuning exhibits saturation behavior; the limiting value is at the dispersionless point – 589.4 nm [30] (**Figure 13**).

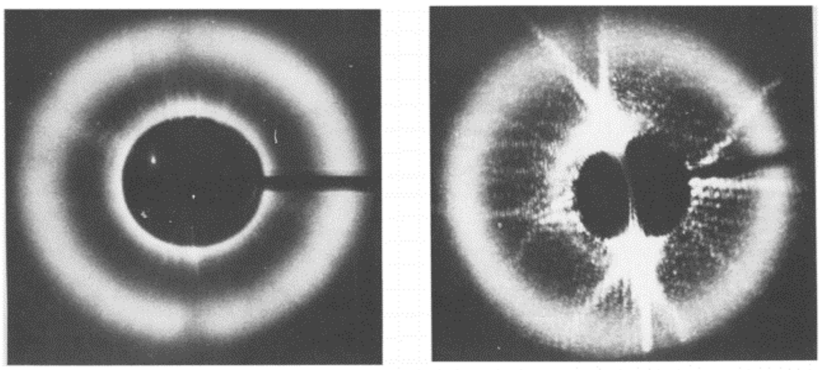

(a) (b)

Figure 13. The pattern of the conical radiation at sodium density 1.8×10^{15} cm^{-3} and laser detuning of 0.2 nm to the blue of the D_2 transition. The laser radiation is focused into the sodium cell by a spherical lens (a) and by a cylindrical lens (b). The laser beam is blocked with a small on-axis disc. The focal line of the cylindrical lens (b) is the long horizontal line [30].

Two kinds of experiments were performed to establish the surface character of the conical emission. The light changes the polarization of the initial beam in a linear case, with a direction that determines the difference between right and left polarizations. Self-trapping of laser light close to the transition is due to saturation effects, and this change in polarization is expected to occur inside the filaments, where the degree of saturation is maximum. In [30], the following conclusion was made: conical radiation is generated in a nonsaturated region such as the self-trapped filament surface.

The control of mechanical effects, such as shock waves, induced by ultrashort laser pulses in water is crucial for applications in biomedicine and material processing [12]. However, optimizing these effects requires a detailed understanding of how laser parameters, particularly pulse duration, influence the underlying energy deposition mechanisms. This study systematically investigates the dependence of shock wave amplitude on fluence (up to 10 J/cm^2) and pulse duration (200 fs to 10 ps) of near-infrared laser pulses under tight focusing conditions (Numerical aperture NA = 0.42), using a combined experimental and numerical approach based on the dynamical rate equation model. Our key finding is that the shock wave amplitude is governed by the total kinetic energy of the electrons in the laser-induced plasma, leading to a distinct maximum at approximately 5 ps (confidence interval: 4.5 - 5.5 ps) and saturation at fluences ~7 J/cm^2. This optimum arises from a balance between the increasing effectiveness of avalanche ionization for longer pulses and the competing effects of electron recombination and reduced photoionization efficiency. Consequently, these results identify a practical parameter window—pulse durations of 4 - 6 ps at moderate fluences—for optimizing laser-induced mechanical effects in applications such as laser surgery in aqueous media.

The attenuation characteristics of a shock wave after optical breakdown in water, with laser pulses of 12-ns duration, are represented in [11]. A high time-resolved shadowgraph method is applied to capture the temporal evolutions of the cavitation bubble wall and shock wave. The experiments are carried out on a single bubble generated far away from the free surface and the rigid walls, with laser pulse energies of 22 mJ, 45 mJ, and 60 mJ. The results show that a high time-resolved wave front velocity of the shock wave is identified, and the maximum velocity can reach up to around 4000 m/s. An asymmetric shock wave is observed at the very start of the bubble expansion stage, and the process of the sharp attenuation of wave front velocity down to sound velocity is accomplished within 310 ns. The possible relationship between the cavitation bubble and the shock wave is discussed, and a prediction model, using the maximum bubble radius and the corresponding time calculated by the Gilmore model, is proposed to calculate the location of the wave front.

Table 3 shows the experimental results for water irradiated with femtosecond lasers with a duration of 340 fs at different wavelengths [14].

Table 3. Threshold for fs optical breakdown in water (340 fs) at different wavelengths λ and NA (numerical aperture), with focal radius $r = 0.61\lambda/\mathrm{NA}$. The threshold values include the breakdown energy E_{th} (50% breakdown probability), irradiance I_{th}, threshold sharpness $S = E_{th}/\Delta E$ where ΔE denotes the interval between 10% and 90% breakdown probability, and the bubble size R_{max} at threshold [27].

λ, nm	NA	r, nm	E_{th}, nJ	I_{th}, 10^{12} W/cm^2	S	R_{max}, nm
1040	0.8	793	22.6	3.37	30.5	328 ± 44
1040	0.9	705	18.5	3.49	18.9	322 ± 96

Continued

520	0.8	397	4.79	2.85	62.3	288 ± 28
520	0.9	353	4.20	3.17	67.8	232 ± 17
347	0.8	264	3.95	5.29	47.1	216 ± 17
347	0.9	235	3.78	6.40	52.2	190 ± 9

As can be seen from Table 3, the maximum radii are in satisfactory agreement with the "electromagnetic" theoretical estimates.

As we can see, the modified Rayleigh model has a general nature and may be applied to estimate the size of voids in all condensed media.

Based on the data in Table 3, it can also be concluded that the decrease in the maximum radius of voids (bubbles) with decreasing wavelength may be due to a decrease in the geometric dimensions of diffraction-stratified cones, and at the same time, Cherenkov cones, and a shift of the Cherenkov radiation spectra into a shorter-wavelength region.

Thus, in all three cases (silicon carbide, potassium chloride, and water), we have the electromagnetic nature of the optical breakdown, which has a complex structure (generation of optically induced Cherenkov radiation and formation of voids), *i.e.*, shock processes.

We now present estimates of the sizes and shapes of possible laser-induced voids for copper and aluminum [17]. For Cu $E = 129.8$ GPa, $\nu = 0.343$, speed of sound 3750 m/s; for aluminum $E = 69$ GPa, $\nu = 0.353$, speed of sound 5000 m/s. Further, we use Formula (13a) and have $R_{maxCu} = 2.15R_{maxSiC}$ and for the electromagnetic case $R^{el}_{maxCu} = 23.7$ nm and for the acoustic case we have $R^{ac}_{maxCu} = \sqrt{\frac{c}{c_{sCu}}}R^{el}_{maxCu} = 280 \times 23.7 \text{ nm} = 6.6 \text{ μm}$. Results for aluminum are next: $R_{maxAl} = 2.95R_{maxSiC}$ and for the electromagnetic case $R^{el}_{maxAl} = 32.5$ nm and for the acoustic case we have $R^{ac}_{maxAl} = \sqrt{\frac{c}{c_{sAl}}}R^{el}_{maxAl} = 245 \times 32.5 \text{ nm} = 8.0 \text{ μm}$. Ellipticity of voids may be estimated with the help of Formula (17) $\alpha_{Cu} = 0.49$ and $\alpha_{Al} = 0.48$.

In this case, we chose the irradiation parameters as for silicon carbide, so these results are of an estimated nature. However, the assessment of the void sizes allows us to determine the mechanism of their formation: electromagnetic (nanovoids) or acoustic (microvoids), which greatly facilitates the choice of modeling methods and the description of the corresponding processes. Thus, this result may be a criterion for determination of the nature of the shock processes.

4. Conclusions

1) The main features and comparative analysis of acoustic and electromagnetic shock processes are observed.

2) Formal similarities and differences between acoustic shock waves and Che-

renkov radiation are shown.

3) Experimental data and the corresponding two-cascade model of acoustic laser-induced shock processes are presented.

4) Some aspects of A. Bohr's microscopic mechanism of Cherenkov radiation and its application in the optical case are discussed.

5) The universality of the five-cascade model, including the modified Rayleigh model, has been tested for acoustic and electromagnetic laser-induced shock processes.

6) The presented experimental results on pulsed laser-induced optical breakdown of silicon carbide, potassium chloride, and water showed that these impact processes are electromagnetic in nature.

7) A criterion for determining the nature of laser-induced shock processes based on the size of voids has been formulated.

Conflicts of Interest

The author declares no conflicts of interest regarding the publication of this paper.

References

[1] Trokhimchuck, P.P. (2026) Relaxed Optics: Modelling and Discussions 4. Lambert Academic Press.

[2] Trokhimchuck, P.P. (2024) Relaxed Optics: Modelling and Discussions 3. Bright Sky Publishing.

[3] Trokhimchuck, P.P. (2026) To the Question about the Nature of Laser-Induced Shock Processes. *Physics and Educational Technologies*, **1**, 112-119.

[4] Trokhimchuck, P.P. (2026) About the Nature of Laser-Induced Shock Processes. *Fiddlehead Journal*, **14**, 77-86. https://doi.org/10.5281/zenodo.19711861

[5] Trokhimchuck, P. (2021) Recent Research and Development Status of Relaxed Optics and Laser Technology: A Review. *Optics and Photonics Journal*, **11**, 210-263. https://doi.org/10.4236/opj.2021.117015

[6] Chandramouli, P.N. (2014) Continuum Mechanics. Yes Dee Publishing Pvt. Ltd.

[7] VonNeumann, J. and Richtmyer, R.D. (1950) A Method for the Numerical Calculation of Hydrodynamic Shocks. *Journal of Applied Physics*, **21**, 232-237. https://doi.org/10.1063/1.1699639

[8] Peyre, P. and Fabbro, R. (1995) Laser Shock Processing: A Review of the Physics and Applications. *Optical and Quantum Electronics*, **27**, 1213-1229. https://doi.org/10.1007/bf00326477

[9] Cao, X., Wu, J., Zhong, G., Wu, J. and Chen, X. (2024) Laser Shock Peening: Fundamentals and Mechanisms of Metallic Material Wear Resistance Improvement. *Materials*, **17**, Article 909. https://doi.org/10.3390/ma17040909

[10] Liu, Q., Chu, S., Zhang, X., Wang, Y., Zhao, H., Zhou, B., *et al.* (2025) Laser Shock Processing of Titanium Alloys: A Critical Review on the Microstructure Evolution and Enhanced Engineering Performance. *Journal of Materials Science & Technology*, **209**, 262-291. https://doi.org/10.1016/j.jmst.2024.04.075

[11] Geng, S., Yao, Z., Zhong, Q., Du, Y., Xiao, R. and Wang, F. (2021) Propagation of Shock Wave at the Cavitation Bubble Expansion Stage Induced by a Nanosecond La-

ser Pulse. *Journal of Fluids Engineering*, **143**, Article 051209. https://doi.org/10.1115/1.4049933

[12] Rishkov, N., Asharchuk, N., Yusupov, V. and Mareev, E. (2025) The Influence of Ultrashort Laser Pulse Duration on Shock Wave Generation in Water under Tight Focusing Conditions. *Photonics*, **12**, 1067-1080. https://doi.org/10.3390/photonics12111067

[13] Fan, Y., Wang, Y., Vukelic, S. and Yao, Y.L. (2005) Wave-Solid Interactions in Laser-Shock-Induced Deformation Processes. *Journal of Applied Physics*, **98**, Article 104904. https://doi.org/10.1063/1.2134882

[14] Frank, I.M. (1988) Vavilov-Cherenkov Radiation. Nauka. (In Russian)

[15] Jelley, J.V. (1958) Čerenkov Radiation and Its Applications. Pergamon Press.

[16] Golub, I. (1990) Optical Characteristics of Supercontinuum Generation. *Optics Letters*, **15**, 305-307. https://doi.org/10.1364/ol.15.000305

[17] Devis, J.R. (1998) Metals Handbook. 2nd Edition, ASM International.

[18] Warren, B.E. (1990) X-Ray Diffraction. Dover Publications, Inc.

[19] Okada, T., Tomita, T., Matsuo, S., Hashimoto, S., Ishida, Y., Kiyama, S., *et al*. (2009) Formation of Periodic Strained Layers Associated with Nanovoids Inside a Silicon Carbide Single Crystal Induced by Femtosecond Laser Irradiation. *Journal of Applied Physics*, **106**, Article 054307. https://doi.org/10.1063/1.3211311

[20] Okada, T., Tomita, T., Matsuo, S., Hashimoto, S., Kashino, R. and Ito, T. (2012) Formation of Nanovoids in Femtosecond Laser-Irradiated Single Crystals of Silicon Carbide. *Materials Science Forum*, **725**, 19-22. https://doi.org/10.4028/www.scientific.net/msf.725.19

[21] Bohr, A. (1948) Atomic Interaction in Penetration Phenomena. *DET KGL Danske Videnskabernes Selskab B Matematisk-Fysiske Meddelelser*, **24**, 1-52.

[22] Rayleigh, L. (1917) On the Pressure Developed in a Liquid during the Collapse of a Spherical Cavity. *The London*, *Edinburgh*, *and Dublin Philosophical Magazine and Journal of Science*, **34**, 94-98. https://doi.org/10.1080/14786440808635681

[23] Lauterborn, W. and Kurz, T. (2010) Physics of Bubble Oscillations. *Reports on Progress in Physics*, **73**, Article 106501. https://doi.org/10.1088/0034-4885/73/10/106501

[24] Couairon, A. and Mysyrowicz, A. (2007) Femtosecond Filamentation in Transparent media. *Physics Reports*, **441**, 47-189. https://doi.org/10.1016/j.physrep.2006.12.005

[25] Sharma, B.S. (1968) Laser-Induced Dielectric Breakdown and Mechanical Damage in Silicate Glasses. Ph.D. Thesis, Simon Fraser University Press.

[26] Yablonovitch, E. (1971) Optical Dielectric Strength of Alkali-Halide Crystals Obtained by Laser-Induced Breakdown. *Applied Physics Letters*, **19**, 495-497. https://doi.org/10.1063/1.1653788

[27] Vogel, A., Linz, N., Freidank, S. and Paltauf, G. (2008) Femtosecond-Laser-Induced Nanocavitation in Water: Implications for Optical Breakdown Threshold and Cell Surgery. *Physical Review Letters*, **100**, Article 038102. https://doi.org/10.1103/physrevlett.100.038102

[28] Fine, R.A. and Millero, F.J. (1973) Compressibility of Water as a Function of Temperature and Pressure. *The Journal of Chemical Physics*, **59**, 5529-5536. https://doi.org/10.1063/1.1679903

[29] Zucker, R.D. and Biblarz, O. (2002) Fundamentals of Gas Dynamics. 2nd Edition, Wiley Books.

[30] Golub, I., Shuker, R. and Erez, G. (1986) On the Optical Characteristics of the Conical

Emission. *Optics Communications*, **57**, 143-145.
https://doi.org/10.1016/0030-4018(86)90145-8

[31] Murzanev, A.A. and Efimenko, E.S. (2018) An Explosion of a Water Droplet Caused by the Ionization of a Substance under the Action of Femtosecond Laser Radiation during Its Filamentation in Air. *Proceedings of the X International Conference Fundamental Problems of Optics*—2018, St. Petersburg, 15-19 October 2018, 3-4. (In Russian)